Spatially resolving density-dependent screening around a single charged atom in graphene

Dillon Wong,[1,2] Fabiano Corsetti,[3] Yang Wang,[1,2] Victor W. Brar,[1,2] Hsin-Zon Tsai,[1,2] Qiong Wu,[1,2] Roland K. Kawakami,[4,5]
Alex Zettl,[1,2,6] Arash A. Mostofi,[3] Johannes Lischner,[3] and Michael F. Crommie[1,2,6,*]

[1]*Department of Physics, University of California at Berkeley, Berkeley California 94720, USA*
[2]*Materials Science Division, Lawrence Berkeley National Laboratory, Berkeley California 94720, USA*
[3]*Department of Materials and Physics, and The Thomas Young Centre for Theory and Simulation of Materials,
Imperial College London, London SW7 2AZ, United Kingdom*
[4]*Department of Physics and Astronomy, University of California, Riverside, California 92521, USA*
[5]*Department of Physics, The Ohio State University, Columbus, Ohio 43210, USA*
[6]*Kavli Energy NanoSciences Institute at the University of California, Berkeley, Berkeley, California 94720, USA
and the Lawrence Berkeley National Laboratory, Berkeley, California 94720, USA*

Electrons in two-dimensional graphene sheets behave as interacting chiral Dirac fermions and have unique screening properties due to their symmetry and reduced dimensionality. By using a combination of scanning tunneling spectroscopy measurements and theoretical modeling we have characterized how graphene's massless charge carriers screen individual charged calcium atoms. A backgated graphene device configuration has allowed us to directly visualize how the screening length for this system can be tuned with carrier density. Our results provide insight into electron-impurity and electron-electron interactions in a relativistic setting with important consequences for other graphene-based electronic devices.

I. INTRODUCTION

Understanding how screening arises from different contributions to the static dielectric function $\epsilon(q)$ is critical for unraveling material-dependent optical [1] and transport properties [2,3], as well as electron-phonon and electron-electron interactions [4,5]. Because it is two-dimensional (2D), graphene provides a unique opportunity to study the effects of screening using spatial imaging techniques while simultaneously employing gate tunability to vary charge-carrier density. The chiral relativistic nature of graphene's charge carriers [6] cause it to have a peculiar screening behavior: Undoped graphene is dielectriclike whereas doped graphene is metal-like [7,8]. Consequently, it is possible to directly image electronic screening processes in graphene over a wide range of different screening regimes.

The screening of charged impurities is of particular importance to the performance of graphene field-effect transistors [3,9]. Charged impurities, for example, can limit carrier mobility [2,10–12], shift the chemical potential [13], induce phase transitions [14–16], create supercritical states [17–20], and split Landau levels [21]. Although interactions between graphene and isolated charged elements, such as adsorbates [22–25] and defects [26,27] have been investigated with local probe techniques, there are currently no spatially resolved studies of the carrier-density dependence of electronic screening of charged impurities in graphene. Here we present a systematic scanning tunneling microscopy (STM) and scanning tunneling spectroscopy study of the local screening response of gate-tunable graphene to individual charged calcium (Ca) adatoms. We find that charged impurities in graphene are screened by chiral Dirac fermions over an atypically long length scale on the order of 10 nm. This screening length is highly dependent

on carrier density and is thus tunable via gate voltage. Our spatially resolved measurements of screening behavior in graphene are in good agreement with theoretical simulations of the electronic response of doped graphene to the presence of a screened Coulomb potential. These results demonstrate the importance of electron-electron interactions (which give rise to screening) for understanding the properties of defects in doped graphene.

II. EXPERIMENTAL RESULTS

We fabricated gate-tunable graphene/boron nitride (BN) devices by growing monolayer graphene via chemical vapor deposition (CVD) [28] and transferring the graphene onto BN crystals [29] exfoliated onto SiO_2/Si wafers. Ca atoms subsequently were deposited onto the surface of our liquid-helium cooled graphene/BN devices in an ultrahigh vacuum chamber (see the Supplemental Material [30] and Ref. [31]). Figure 1(a) depicts the graphene device used in our experimental setup. Figure 1(b) shows a typical STM topographic image of graphene following this Ca deposition procedure.

To determine the charge state of the Ca atoms at different doping levels we performed gate-dependent dI/dV spectroscopy on graphene at various distances away from an isolated Ca atom (i.e., a Ca atom separated by at least 20 nm from all other Ca atoms). These data are plotted in Figs. 2(a)–2(c) for p-doped, nearly neutral, and n-doped graphene. Each dI/dV curve here has been normalized by a different constant to account for the exponential dependence of the tunneling conductance on tip height [23]. All dI/dV curves show a $\sim$130-meV-wide gaplike feature at the Fermi level caused by phonon-assisted inelastic tunneling [32,33], and the p-doped (n-doped) spectra exhibit local minima on the right (left) side of the Fermi level that reflect the graphene Dirac point (E_D). For the nearly neutral graphene spectra, E_D is near the Fermi level, and its location is obscured by the gaplike feature.
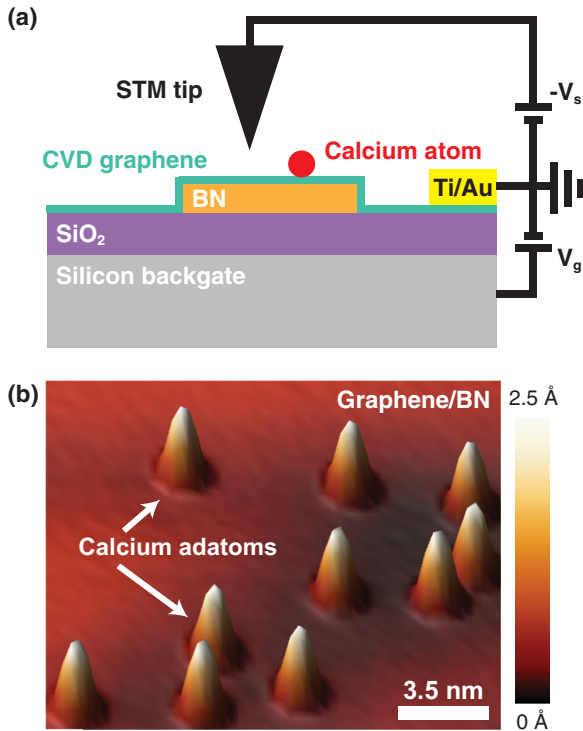
*crommie@berkeley.edu

(a)

(b)

FIG. 1. (a) Schematic of the experimental setup. Calcium atoms are deposited onto a graphene/BN/SiO$_2$/Si device. A voltage V_g is applied to Si to tune the charge-carrier density in graphene, and a voltage $-V_s$ is applied to the STM tip. (b) STM topographic image of Ca atoms adsorbed onto a graphene/BN surface.

The dI/dV curves in Figs. 2(a)–2(c) all display an electron-hole asymmetry in which the dI/dV intensity at energies above E_D increases as the STM tip approaches the Ca atom, whereas the dI/dV intensity at energies below E_D decreases as the tip approaches the Ca atom. This observation is consistent with previous theoretical predictions that the local density of states (LDOS) of graphene increases for energies above E_D and decreases for energies below E_D as one approaches a positively charged Coulomb center [18,19]. We thus conclude that the Ca atom is positively charged and stable regardless of the graphene doping level within our experimental conditions. dI/dV spectra taken directly above individual Ca atoms confirm that there are no electronic resonances of the atom in the energy range near the Fermi level explored here, consistent with the charge stability displayed in Figs. 2(a)–2(c) (see the Supplemental Material [30]). Additionally, the electric fields involved in this experiment are too low to cause Ca to transition to a metastable state exhibiting different charges [34].

The charge stability of Ca atoms for different gating conditions allows us to image graphene's screening response to charged impurities over a wide range of doping levels. Figures 3(a)–3(c) show gate-dependent dI/dV maps near a Ca atom as the p doping in graphene progressively is increased by ramping up the gate voltage [the sample bias (V_s) was changed at each gate voltage (V_g) to ensure that only electronlike states 0.15 eV above E_D were tracked in all three dI/dV maps]. We chose to image states 0.15 eV above E_D to avoid the additional complication of quasiparticle interference

in these measurements. Figure 3(a) shows the dI/dV map at the smallest gate voltage where the graphene has a p-type charge-carrier density of $\sim 3 \times 10^{11}\,\mathrm{cm}^{-2}$. The yellow region shows the increased electronlike LDOS that occurs as graphene charge carriers rearrange themselves in response to the screened Coulomb potential of the positively charged Ca atom. Figures 3(b) and 3(c) show the same region of graphene after raising the density of p-type charge carriers to $\sim 1.8 \times 10^{12}$ and $\sim 3.5 \times 10^{12}\,\mathrm{cm}^{-2}$, respectively. The yellow region is seen to decrease in size as the increased carrier density more effectively screens the Ca atom and reduces the range of its associated Coulomb potential. To more accurately quantify these trends, we measured dI/dV line scans as a function of distance from the Ca atom. These line scans [Fig. 3(d)] show that the characteristic decay length of the LDOS decreases as the p-type graphene carrier density increases.

Figures 4(a)–4(c) show dI/dV maps of the same region as Fig. 3 but for different n-doping carrier densities and for holelike states 0.08 eV below E_D (energies on opposite sides of E_D were chosen for n- and p-doped graphene to avoid the phonon gaplike feature, thereby allowing states to be characterized with greater precision). Figure 4(a) shows the graphene response to a single Ca atom for the smallest number of n-type charge carriers: $\sim 0.5 \times 10^{11}\,\mathrm{cm}^{-2}$. Since states below E_D are imaged here the contrast is flipped compared to the images of Figs. 3(a)–3(c) (we emphasize that this is not a result of the polarity of charge carriers in graphene). Figures 4(b) and 4(c) show how the n-type screening response to the Ca atom increases as carrier density is ramped up to $\sim 1.4 \times 10^{12}\,\mathrm{cm}^{-2}$. The blue region is seen to shrink as the Coulomb potential range reduces with increased screening. As seen in the dI/dV line scans in Fig. 4(d), the presence of the Ca atom strongly reduces the graphene LDOS near the atom, but the LDOS returns to its unperturbed value at long distances. The length scale over which this occurs (i.e., the screening length) is seen to decrease for increased n-type carrier densities, similar to what is observed in the case of p-type carrier densities [Fig. 3(d)].

III. THEORETICAL SIMULATIONS

Our observation that the decay length of dI/dV decreases with increasing carrier concentration can be understood qualitatively via Thomas-Fermi (TF) screening theory. In three-dimensional (3D) metals the static wave-vector- (q-) dependent Thomas-Fermi dielectric function is

$$\epsilon_{3D}(q) = 1 + \frac{4\pi e^2 \mathrm{DOS}(E_F)}{q^2}, \qquad (1)$$

where $\mathrm{DOS}(E_F)$ is the density of states at the Fermi energy. However, screening in 2D materials is typically weaker (resulting in stronger Coulomb interactions) because electric-field lines can leave the plane of a 2D material [35]. The 2D Thomas-Fermi dielectric function is [6,7,36,37]

$$\epsilon_{2D}(q) = \epsilon_s + \frac{1}{\lambda_{\mathrm{TF}} q}, \qquad (2)$$

where ϵ_s is the effective substrate dielectric constant and

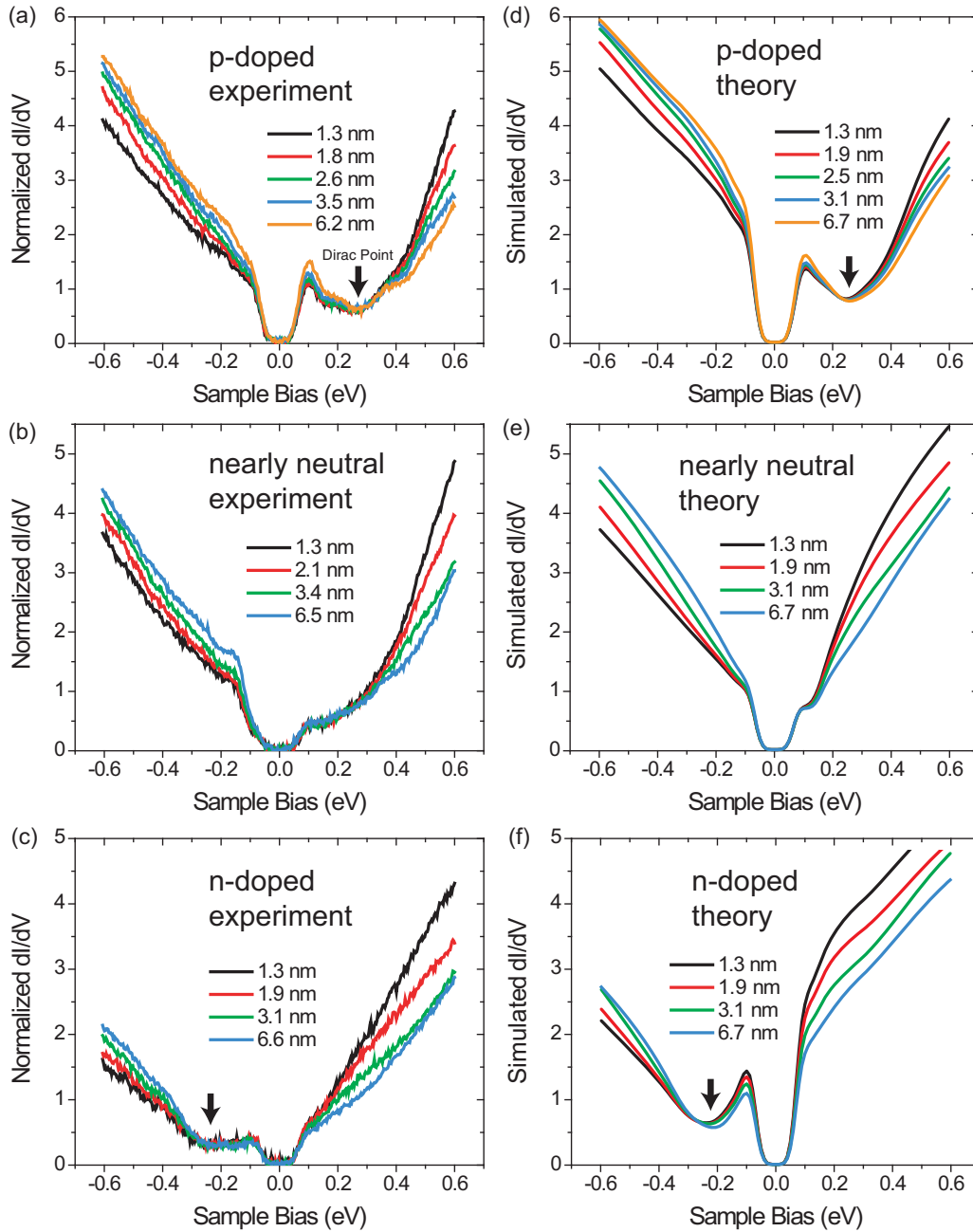$$\lambda_{\mathrm{TF}} = \frac{1}{2\pi e^2 \mathrm{DOS}(E_F)} \qquad (3)$$

FIG. 2. (a)–(c) dI/dV point spectra measured at different distances from a single Ca atom on p-doped, nearly neutral, and n-doped graphene. These dI/dV spectra show that a Ca atom on graphene remains positively charged as graphene's charge-carrier density is tuned via a backgate voltage V_{g}. (d)-(e) Tight-binding simulation of dI/dV spectra at different distances from a screened Coulomb potential on p-doped, nearly neutral, and n-doped graphene. The Dirac points are indicated by black arrows.

is the Thomas-Fermi screening length [8]. Unlike a conventional 2D electron gas that has DOS(E_F) independent of the charge-carrier density n [38], graphene has a carrier-density-dependent electronic density of states and thus a carrier-density-dependent Thomas-Fermi screening length,

$$\lambda_{\mathrm{TF}} = \frac{\hbar v_F}{4e^2 \sqrt{\pi |n|}}, \qquad (4)$$

where v_{F} is the magnitude of the Fermi velocity. λ_{TF} depends sensitively on $|n|$ and therefore can be tuned by application of a gate voltage. Increasing the magnitude of the carrier

density via the gate voltage V_{g} thus leads to a decrease in λ_{TF}, which explains the observed decrease in the decay length of dI/dV for both p-doped (Fig. 3) and n-doped (Fig. 4) graphene.

This simple Thomas-Fermi screening picture, however, has several shortcomings. First, it does not include the effect of interband transitions between graphene's π and π^* bands. Second, the Thomas-Fermi theory is only valid for slowly varying potentials and for energies far from the graphene Dirac point. Third, it does not directly predict the electronic LDOS, which is most closely related to the experimentally
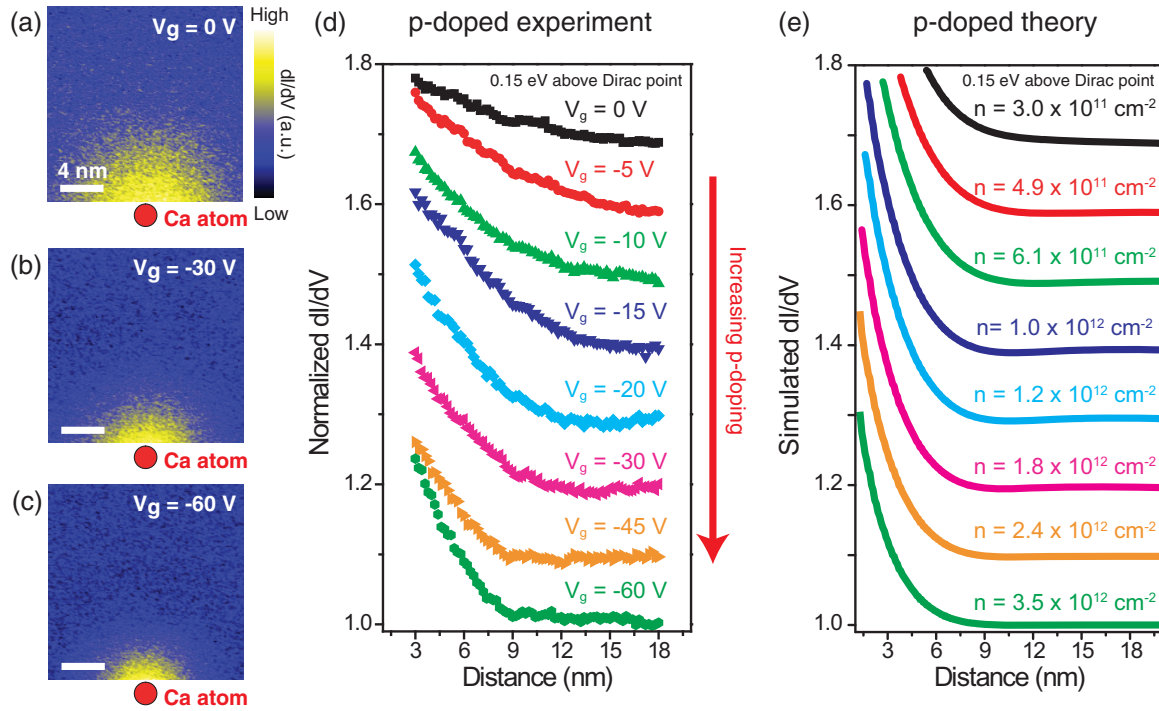
FIG. 3. (a)–(c) dI/dV maps 0.15 eV above the Dirac point near a single Ca atom (represented by the red disk) on *p*-doped graphene at $V_g = 0, -30$, and -60 V (the Ca atom was not directly scanned to minimize the risk of picking the atom up with the STM tip). (d) Radially averaged dI/dV line cuts of electronic states 0.15 eV above the Dirac point as a function of distance from a single Ca atom on *p*-doped graphene. The curves are vertically offset for clarity with the magnitude of *p* doping increasing from the top curve to the bottom curve. (e) Theoretical dI/dV line cuts (simulated via tight binding) of electronic states 0.15 eV above the Dirac point as a function of distance from a RPA-screened Coulomb potential on *p*-doped graphene. Carrier-density values for each line cut are calculated from the position of the Dirac point observed experimentally for the measurements shown in (d). The value of dI/dV far from the Ca atom is set to 1 in (d) and (e).
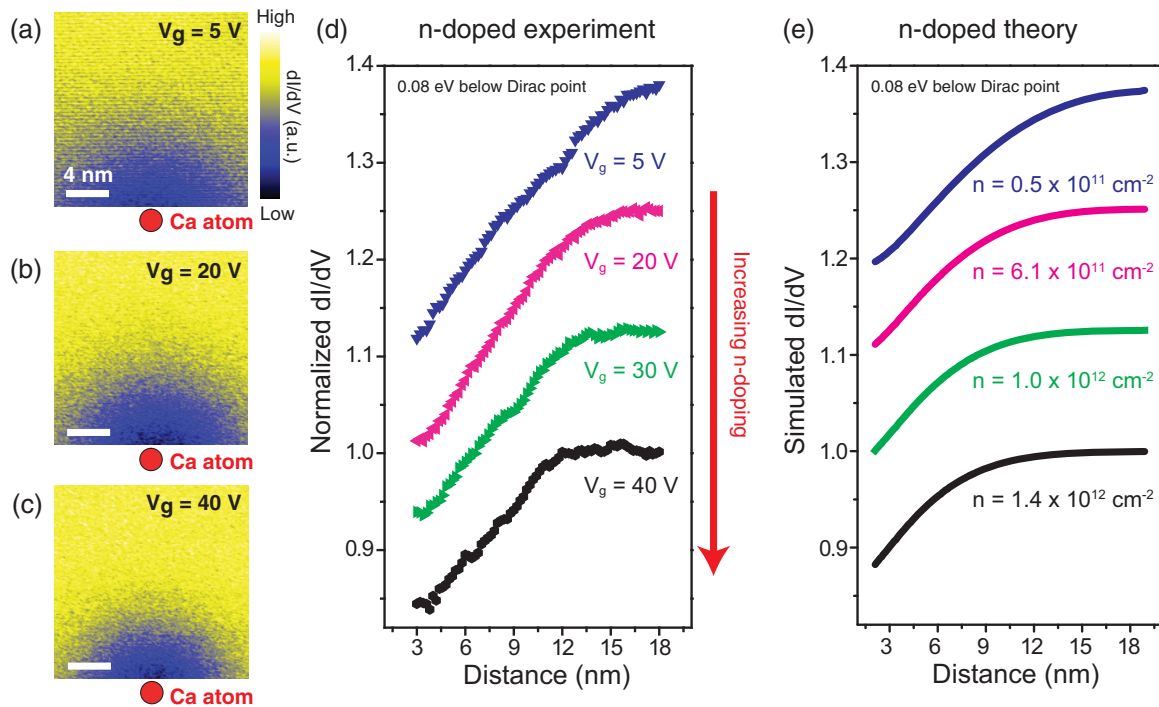

FIG. 4. (a)–(c) dI/dV maps 0.08 eV below the Dirac point near a single Ca atom on *n*-doped graphene at $V_g = 5, 20$, and 40 V. (d) Radially averaged dI/dV line cuts of electronic states 0.08 eV below the Dirac point as a function of distance from a single Ca atom on *n*-doped graphene. (e) Simulated dI/dV line cuts of electronic states 0.08 eV below the Dirac point as a function of distance from a RPA-screened Coulomb potential on *n*-doped graphene.

measured quantity dI/dV. Therefore, to more quantitatively and realistically explain our STM measurements, we carried out theoretical calculations for a doped graphene sheet with a single Ca adatom. We used a nearest-neighbor tight-binding model of carbon p_z orbitals to describe the electronic structure

of graphene with the addition of a screened Coulomb potential as an on-site term to reproduce the effect of the Ca adatom. Here the bare Coulomb potential is screened using the random phase approximation (RPA) dielectric function for the Dirac Hamiltonian [7,39],

$$\epsilon(q) = \begin{cases} \epsilon_s + \frac{2\pi e^2 \mathrm{DOS}(E_F)}{q}, & q \leqslant 2k_F, \\ \epsilon_s + \frac{2\pi e^2 \mathrm{DOS}(E_F)}{q}\left[1 - \frac{1}{2}\sqrt{1 - \left(\frac{2k_F}{q}\right)^2} + \frac{q}{4k_F}\cos^{-1}\frac{2k_F}{q}\right], & q > 2k_F, \end{cases} \tag{5}$$

where k_F is the magnitude of the Fermi wave vector with respect to the K/K' points. The effect of changing charge-carrier density in our tight-binding calculations is introduced through the dielectric function of Eq. (5). We use the following parameters in our simulation: the graphene carbon-carbon bond length $a = 0.142$ nm, $v_F = 1.1 \times 10^6$ m/s, $\epsilon_s = 2.5$, the impurity charge $Q = +0.7|e|$ (see the Supplemental Material [30]), and the height $h = 2.0$ Å of the Ca atom above the center of the graphene hexagon [40].

Figures 2(d)–2(f) show the results of our simulated dI/dV point spectra for p-doped, nearly neutral, and n-doped graphene (each colored curve corresponds to a different distance from the Ca atom). Quasiparticle lifetime effects and inelastic tunneling processes have been included (see Ref. [33] for details on this procedure; the Supplemental Material [30] shows theoretical curves without lifetime and inelastic tunneling effects). In agreement with the experimental data Figs. 2(a)–2(c), the computed spectra exhibit a significant electron-hole asymmetry when the tip is brought closer to the adatom; the simulated LDOS increases above the Dirac point and decreases below the Dirac point for closer distances.

An intuitive picture for understanding these findings is that the LDOS of graphene in the presence of the charged impurity is described by the LDOS of unperturbed graphene but shifted towards lower energies by the local value of the screened Coulomb potential. This explains the reduction of dI/dV below E_D and its increase above E_D. We find that a shifted LDOS is in good agreement with our calculations for energies sufficiently far from the Dirac point (see the Supplemental Material [30]). In the vicinity of the Dirac point, however, this intuitive picture breaks down. In particular, the Dirac point itself does not shift in energy—a consequence of the linear dispersion of the graphene Dirac bands [18].

To model our experimental dI/dV maps and better visualize the spatial dependence of the screening behavior we calculated the theoretical tunneling conductance as a function of distance away from a Ca adatom at fixed energy. Figures 3(e) and 4(e) show simulated dI/dV versus distance for p-doped and n-doped graphene, respectively. The energies and charge-carrier densities n were chosen such that Fig. 3(e) directly corresponds to Fig. 3(d) and Fig. 4(e) directly corresponds to Fig. 4(d). In agreement with the experimental results shown in Figs. 3(d) and 4(d), the theoretical spatial profile of the tunnel conductance decays more rapidly for higher doping levels (for both p-doped and n-doped graphene), directly reflecting the reduced range of the impurity potential caused by a reduced screening length. We also carried out large-scale first-principles calculations of the calcium-graphene system within

a density functional theory framework as implemented in the ONETEP code [41,42], which confirm the trends obtained from the tight-binding model (see the Supplemental Material [30]).

IV. CONCLUSIONS

These results directly confirm that the RPA model correctly describes screening by relativistic charge carriers in graphene. RPA screening already has played an essential role in early theoretical models of bipolar electron transport in graphene as it explains the V-shaped conductivity as a function of gate voltage [43–45]. Screening of charged impurities causes long-range impurity scattering to dominate graphene's transport properties at low carrier concentrations and short-range impurity scattering to dominate at high carrier concentrations [2]. Our data for the simplest possible charged-impurity system—a single isolated impurity on graphene–allows us to directly visualize this phenomenon and quantitatively test these assumptions. A closer comparison between our experimental data and simulations reveals that there are discrepancies between our observations and the results of linear-response theory. Indeed, RPA-calculated LDOS near a charged impurity appears to return to its unperturbed value more quickly than the experimental dI/dV response (see the Supplemental Material [30] for a quantitative comparison). This indicates the limitations of RPA, beyond which nonlinear corrections [9,46] or a new theory for electron-electron interactions are required. Nevertheless, the fundamental behavior described here can be generalized to gain insight into the screening of other electrostatic potentials, such as graphene pn junctions [47–50], quantum dots [51,52], and superlattices [53–59] where the potential landscape felt by graphene charge carriers is altered by density-dependent screening effects. Data concerning this paper can be accessed in Ref. [60].

[1] M. Rohlfing and S. G. Louie, Phys. Rev. B **62**, 4927 (2000).
[2] S. Das Sarma, S. Adam, E. H. Hwang, and E. Rossi, Rev. Mod. Phys. **83**, 407 (2011).
[3] E. H. Hwang and S. Das Sarma, Phys. Rev. B **79**, 165404 (2009).
[4] V. Z. Kresin and S. A. Wolf, Rev. Mod. Phys. **81**, 481 (2009).
[5] V. N. Kotov, B. Uchoa, V. M. Pereira, F. Guinea, and A. H. Castro Neto, Rev. Mod. Phys. **84**, 1067 (2012).
[6] A. H. Castro Neto, F. Guinea, N. M. R. Peres, K. S. Novoselov, and A. K. Geim, Rev. Mod. Phys. **81**, 109 (2009).
[7] E. H. Hwang and S. Das Sarma, Phys. Rev. B **75**, 205418 (2007).
[8] D. A. Siegel, W. Regan, A. V. Fedorov, A. Zettl, and A. Lanzara, Phys. Rev. Lett. **110**, 146802 (2013).
[9] M. I. Katsnelson, Phys. Rev. B **74**, 201401 (2006).
[10] J. H. Chen, C. Jang, S. Adam, M. S. Fuhrer, E. D. Williams, and M. Ishigami, Nat. Phys. **4**, 377 (2008).
[11] K. Pi, K. M. McCreary, W. Bao, W. Han, Y. F. Chiang, Y. Li, S. W. Tsai, C. N. Lau, and R. K. Kawakami, Phys. Rev. B **80**, 075406 (2009).
[12] K. M. McCreary, K. Pi, A. G. Swartz, W. Han, W. Bao, C. N. Lau, F. Guinea, M. I. Katsnelson, and R. K. Kawakami, Phys. Rev. B **81**, 115453 (2010).
[13] L. Zhao *et al.*, Science **333**, 999 (2011).
[14] K. C. Rahnejat, C. A. Howard, N. E. Shuttleworth, S. R. Schofield, K. Iwaya, C. F. Hirjibehedin, C. Renner, G. Aeppli, and M. Ellerby, Nat. Commun. **2**, 558 (2011).
[15] S. Ichinokura, K. Sugawara, A. Takayama, T. Takahashi, and S. Hasegawa, ACS Nano **10**, 2761 (2016).
[16] J. Chapman, Y. Su, C. A. Howard, D. Kundys, A. N. Grigorenko, F. Guinea, A. K. Geim, I. V. Grigorieva, and R. R. Nair, Sci. Rep. **6**, 23254 (2016).
[17] Y. Wang *et al.*, Science **340**, 734 (2013).
[18] V. M. Pereira, J. Nilsson, and A. H. Castro Neto, Phys. Rev. Lett. **99**, 166802 (2007).
[19] A. V. Shytov, M. I. Katsnelson, and L. S. Levitov, Phys. Rev. Lett. **99**, 246802 (2007).
[20] J. Mao, Y. Jiang, D. Moldovan, G. Li, K. Watanabe, T. Taniguchi, M. R. Masir, F. M. Peeters, and E. Y. Andrei, Nat. Phys. **12**, 545 (2016).
[21] A. Luican-Mayer, M. Kharitonov, G. Li, C.-P. Lu, I. Skachko, A.-M. B. Gonçalves, K. Watanabe, T. Taniguchi, and E. Y. Andrei, Phys. Rev. Lett. **112**, 036804 (2014).
[22] V. W. Brar *et al.*, Nat. Phys. **7**, 43 (2011).
[23] Y. Wang, V. W. Brar, A. V. Shytov, Q. Wu, W. Regan, H.-Z. Tsai, A. Zettl, L. S. Levitov, and M. F. Crommie, Nat. Phys. **8**, 653 (2012).
[24] H.-Z. Tsai *et al.*, ACS Nano **9**, 12168 (2015).
[25] S. Wickenburg *et al.*, Nat. Commun. **7**, 13553 (2016).
[26] D. Wong *et al.*, Nat. Nanotechnol. **10**, 949 (2015).
[27] J. Velasco *et al.*, Nano Lett. **16**, 1620 (2016).
[28] X. Li *et al.*, Science **324**, 1312 (2009).
[29] C. R. Dean *et al.*, Nat. Nanotechnol. **5**, 722 (2010).
[30] See Supplemental Material at http://link.aps.org/supplemental/10.1103/PhysRevB.95.205419 for methods and additional data.
[31] H. S. Jung *et al.*, J. Visualized Exp. **101**, e52711 (2015).
[32] Y. Zhang, V. W. Brar, F. Wang, C. Girit, Y. Yayon, M. Panlasigui, A. Zettl, and M. F. Crommie, Nat. Phys. **4**, 627 (2008).
[33] V. W. Brar, S. Wickenburg, M. Panlasigui, C.-H. Park, T. O. Wehling, Y. Zhang, R. Decker, Ç. Girit, A. V. Balatsky, S. G. Louie, A. Zettl, and M. F. Crommie, Phys. Rev. Lett. **104**, 036805 (2010).
[34] W. Steurer, J. Repp, L. Gross, I. Scivetti, M. Persson, and G. Meyer, Phys. Rev. Lett. **114**, 036801 (2015).
[35] P. Cudazzo, I. V. Tokatly, and A. Rubio, Phys. Rev. B **84**, 085406 (2011).
[36] T. Ando, J. Phys. Soc. Jpn. **75**, 074716 (2006).
[37] T. Sohier, M. Calandra, and F. Mauri, Phys. Rev. B **91**, 165428 (2015).
[38] S. Adam and S. Das Sarma, Phys. Rev. B **77**, 115436 (2008).
[39] B. Wunsch, T. Stauber, F. Sols, and F. Guinea, New J. Phys. **8**, 318 (2006).
[40] K. T. Chan, J. B. Neaton, and M. L. Cohen, Phys. Rev. B **77**, 235430 (2008).
[41] C.-K. Skylaris, P. D. Haynes, A. A. Mostofi, and M. C. Payne, J. Chem. Phys. **122**, 084119 (2005).
[42] F. Corsetti, A. A. Mostofi, and J. Lischner, 2D Mater. **4**, 025070 (2017).
[43] E. H. Hwang, S. Adam, and S. Das Sarma, Phys. Rev. Lett. **98**, 186806 (2007).
[44] K. Nomura and A. H. MacDonald, Phys. Rev. Lett. **98**, 076602 (2007).
[45] S. Adam, E. H. Hwang, V. M. Galitski, and S. Das Sarma, Proc. Natl. Acad. Sci. U.S.A. **104**, 18392 (2007).
[46] M. Ghaznavi, Z. L. Mišković, and F. O. Goodman, Phys. Rev. B **81**, 085416 (2010).
[47] A. F. Young and P. Kim, Nat. Phys. **5**, 222 (2009).
[48] N. Stander, B. Huard, and D. Goldhaber-Gordon, Phys. Rev. Lett. **102**, 026807 (2009).
[49] L. M. Zhang and M. M. Fogler, Phys. Rev. Lett. **100**, 116804 (2008).
[50] G.-H. Lee, G.-H. Park, and H.-J. Lee, Nat. Phys. **11**, 925 (2015).
[51] Y. Zhao *et al.*, Science **348**, 672 (2015).
[52] J. Lee *et al.*, Nat. Phys. **12**, 1032 (2016).
[53] M. Yankowitz, J. Xue, D. Cormode, J. D. Sanchez-Yamagishi, K. Watanabe, T. Taniguchi, P. Jarillo-Herrero, P. Jacquod, and B. J. LeRoy, Nat. Phys. **8**, 382 (2012).

[54] C. R. Dean *et al.*, Nature (London) **497**, 598 (2013).

[55] B. Hunt *et al.*, Science **340**, 1427 (2013).

[56] L. A. Ponomarenko *et al.*, Nature (London) **497**, 594 (2013).

[57] G. Li, A. Luican, J. M. B. Lopes dos Santos, A. H. Castro Neto, A. Reina, J. Kong, and E. Y. Andrei, Nat. Phys. **6**, 109 (2010).

[58] D. Wong, Y. Wang, J. Jung, S. Pezzini, A. DaSilva, H.-Z. Tsai, H. S. Jung, R. Khajeh, Y. Kim, J. Lee, S. Kahn, S. Tollabimazraehno, H. Rasool, K. Watanabe, T. Taniguchi, A. Zettl, S. Adam, A. H. MacDonald, and M. F. Crommie, Phys. Rev. B **92**, 155409 (2015).

[59] C.-H. Park, L. Yang, Y.-W. Son, M. L. Cohen, and S. G. Louie, Nat. Phys. **4**, 213 (2008).

[60] Data underlying this article can be accessed on figshare at https://dx.doi.org/10.6084/m9.figshare.3824451 and used under the Creative Commons Attribution license.